Fast, Na^+/K^+ Pump Driven, Steady-State Transcytolemmal Water Exchange in Neuronal Tissue: A Study of Rat Brain Cortical Cultures

Ruiliang Bai,[1] Charles S. Springer, Jr.,[2] Dietmar Plenz,[3] and Peter J. Basser[1]*

Purpose: Water homeostasis and transport play important roles in brain function (e.g., ion homeostasis, neuronal excitability, cell volume regulation, etc.). However, specific mechanisms of water transport across cell membranes in neuronal tissue have not been completely elaborated.

Methods: The kinetics of transcytolemmal water exchange were measured in neuronal tissue using simultaneous, real-time fluorescence and nuclear magnetic resonance (NMR) measurements of perfused, active brain organotypic cortical cultures. Perfusion with a paramagnetic MRI contrast agent, gadoteridol, allows NMR determination of the unidirectional rate constant for steady-state cellular water efflux (k_{io}), and the mole fraction of intracellular water (p_i), related to the average cell volume (V). Changes in intracellular calcium concentration $[Ca_i^{2+}]$ were used as a proxy for neuronal activity and were monitored by fluorescence imaging.

Results: The k_{io} value, averaged over all cultures ($N = 99$) at baseline, was 2.02 (± 1.72) s^{-1}, indicating that on average, the equivalent of the entire intracellular water volume turns over twice each second. To probe possible molecular pathways, the specific Na^+-K^+-ATPase (NKA) inhibitor, ouabain (1 mM), was transiently introduced into the perfusate. This caused significant transient changes ($N = 8$): $[Ca_i^{2+}]$ rose ~250%, V rose ~89%, and k_{io} fell ~45%, with a metabolically active k_{io} contribution probably eliminated by ouabain saturation.

Conclusions: These results suggest that transcytolemmal water exchange in neuronal tissue involves mechanisms affected by NKA activity as well as passive pathways. The active pathway may account for half of the basal homeostatic water flux. **Magn Reson Med 79:3207–3217, 2018. © 2017 International Society for Magnetic Resonance in Medicine.**

Key words: transcytolemmal water exchange; steady-state; neurons; active; Na^+/K^+ pump; ouabain

INTRODUCTION

Water balance and transport play important roles in maintaining homeostasis and tissue function in the brain. Water flow and/or exchange continuously mixes water pools in the brain—within the blood, cerebrospinal fluid, and brain parenchyma's intracellular and interstitial spaces. This phenomenon plays a critical role in brain function (e.g., regulating cell volume and ion balance, astrocyte migration, neuroexcitation, etc.) (1–4). Abnormal water transport is observed in, or is the major contributor to, a variety of brain diseases and disorders, including cerebral edema, stroke, traumatic brain injury (5–7).

Although the importance of water transport in the nervous system is well known, our ability to measure or detect it is limited. Exactly how water is transported across cell membranes, a fundamental issue in biology, has not been completely elaborated. For example, how rapidly is water transported between intracellular cytoplasm and the interstitium in neurons and glia? Is this transport process passive (i.e., diffusion driven), active, or both? Does water transport adapt or change in some pathological conditions (e.g., edema, traumatic brain injury)? These are a few of the questions this study begins to address.

Cells swell or shrink because of a net influx or efflux of water, respectively, in response to an osmotic gradient (8). Since the earliest transcytolemmal water transport studies, however, it has been known that the time constants for these net fluxes (seconds or minutes) are longer than those for steady-state water exchange across the cell membrane (milliseconds) (9). It has been generally assumed this exchange process is energetically passive. At first, it was thought to be simple unfacilitated water diffusion across the phospholipid bilayer (Fig. 1). Later, when water channel membrane proteins, aquaporins (AQPs), were discovered, this exchange was thought to be facilitated, although still passive.

More recently, it was suggested there is also an energetically active component to transcytolemmal water exchange (10,11). The hypothesis is that this active component is largely driven by the cell membrane Na^+-K^+-ATPase pump (NKA), the cell's major active transporter (11,12). This ubiquitous enzyme transports three Na^+ ions outward and two K^+ ions inward, for every ATP molecule hydrolyzed, to maintain ion concentration gradients and the transcytolemmal potential (13). There are, of course, transporters that K^+ uses to re-exit (Fig. 1, II) and Na^+ to re-enter (Fig. 1, III) the cell; this requires continual NKA "turnover" (see below). Accompanying this ion cycling,

[1]Section on Quantitative Imaging and Tissue Sciences, DIBGI, NICHD, National Institutes of Health, Bethesda, Maryland, USA.

[2]Advanced Imaging Research Center, Oregon Health & Science University, Portland, Oregon, USA.

[3]Section on Critical Brain Dynamics, LSN, NIMH, National Institutes of Health, Bethesda, Maryland, USA.

Grant sponsor: Eunice Kennedy Shriver National Institute of Child Health and Human Development; Grant number: Intramural Research Program; Grant sponsor: NIH; Grant numbers: UO1-CA154602 and R44-CA180425; Grant sponsor: Paul G. Allen Family Foundation; Grant number: 12079; Grant sponsor: National Institute of Mental Health, NIH; Grant number: Intramural Research Program (IRP).

*Correspondence to: Peter J. Basser, Ph.D., Section on Quantitative Imaging and Tissue Sciences, DIBGI, NICHD, National Institutes of Health, Bethesda, MD 20892, USA. E-mail: basserp@helix.nih.gov

Received 11 July 2017; revised 1 October 2017; accepted 2 October 2017
DOI 10.1002/mrm.26980
Published online 6 November 2017 in Wiley Online Library (wileyonlinelibrary.com).

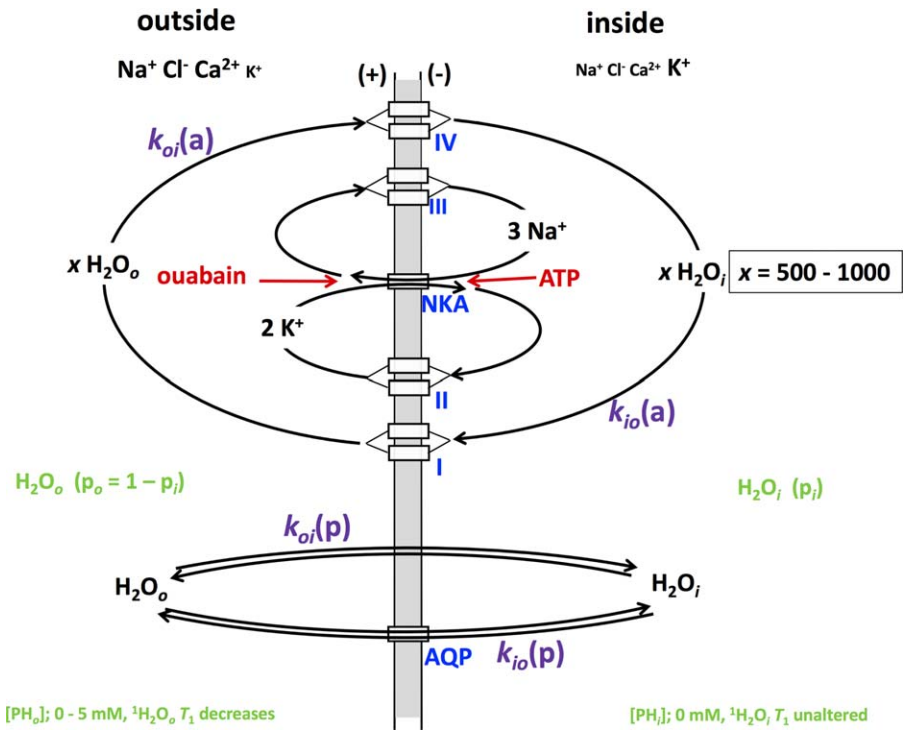

FIG. 1. Illustration of the passive (p) and potentially active (a) transcytolemmal water exchange pathways in biological tissue. k_{io} and k_{oi} are the steady-state cellular water efflux and influx rate constants, respectively. II and III represent transporters K^+ uses to re-exit and Na^+ uses to re-enter the cell, respectively. I and IV represent water co-transporters that H_2O uses to exit and enter the cell, respectively. The subscripts "*o*" and "*i*" represent outside and inside the cell respectively, p_o and p_i, the respective mole fractions of extra- and intracellular water; PH, the MRI contrast agent ProHance, and T_1, the ^1H_2O signal longitudinal relaxation rate constant. The Na^+,K^+-ATPase (NKA) substrate ATP_i and inhibitor ouabain are also indicated, in red.

water is thought to use one or several secondary active cotransporters (Fig. 1, I) to exit the cell and one or several cotransporters (Fig. 1, IV) to enter the cell—active transcytolemmal water cycling—each having large water stoichiometry ($x = 500$–1000, Fig. 1) (14), possibly even greater for the overall process (x, in pmol(H_2O)/pmol(ATP)) (12). Although alone it is passive, AQP has been found to sometimes co-localize with NKA (15). This could enable an NKA/AQP complex to function as an active water co-transporter, although likely with a smaller x (<200) than the known water co-transporters.

In this work, we studied transcytolemmal water exchange kinetics in neuronal tissue. To achieve this, we used an MR method to quantify the transcytolemmal water exchange kinetics in a live brain cortical tissue model—rat brain organotypic cortical cultures (OCC)—in both a normal and a pathological condition. The latter entailed reducing NKA pump activity by briefly perfusing with high concentration ouabain. By perfusing OCC with a paramagnetic MRI contrast agent, gadoteridol (ProHance, PH), simultaneous NMR measurements of the unidirectional rate constant for steady-state cellular water efflux, k_{io}, and the mole fraction of sample intracellular water, p_i, could be carried out. The intracellular calcium concentration was also simultaneously monitored via fluorescence microscopy of the same specimen to assess the Ca^{2+} dynamics and neuronal activity in OCC.

METHODS

Transcytolemmal Water Exchange Pathways

According to the hypothesis, the rate constant, k_{io} has two additive components:

$$k_{io} = k_{io}(\mathrm{a}) + k_{io}(\mathrm{p}), \qquad [1]$$

where a and p represent the active and passive k_{io} contributions, respectively. For passive exchange, $k_{io}(\mathrm{p}) = \langle A/V\rangle \times P_W(\mathrm{p})$, where $\langle A/V\rangle$ is the mean cell surface area/volume ratio, and $P_W(\mathrm{p})$ is the diffusion-driven passive membrane water permeability coefficient (10,11). The active rate constant, $k_{io}(\mathrm{a})$, depends on the cellular metabolic rate of NKA, ${}^cMR_{NKA}$ (e.g., pmol(ATP)/s/cell). Therefore, we rewrite k_{io} as:

$$k_{io} = \{x/[\mathrm{H_2O}_i]/\langle V\rangle\}{}^cMR_{NKA} + \langle A/V\rangle \times P_W(\mathrm{p}), \qquad [2]$$

where $[H_2O_i]$ is the intracellular water concentration, which is generally regulated (16) at 30 M (e.g., pmol/pL) (17). To date, there has been no means to measure ${}^cMR_{NKA}$ in vivo, let alone map it with high-resolution (10,11), so the proposed method described below represents an important potential opportunity for its direct measurement via MRI.

OCC

Organotypic brain tissue cultures were prepared from acute coronal somatosensory cortex slices of newborn rats (postnatal days 1–3, Sprague-Dawley), with a protocol approved by the NIMH Animal Care and Use Committee. For each study, two acute slices (350-μm thickness each) were attached to a #1 coverslip by using a plasma–thrombin mixture, submerged in 800 μL of culture medium, and incubated at 35.0°C (±0.5°C). The medium was replaced every 3 to 4 days. Cultures were grown for 2 to 3 weeks before being used in experiments (for details see 18,19). There is no vasculature in these tissues, so that vascular coupling, cardiac pulsation,

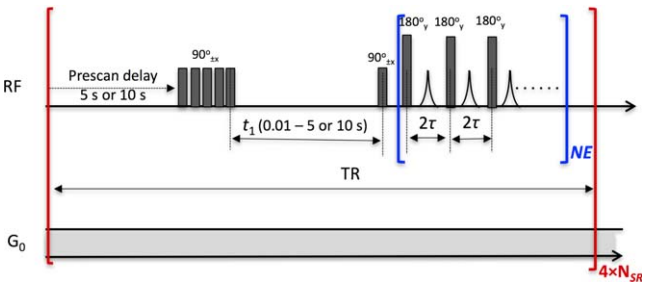

FIG. 2. The saturation recovery (SR) pulse sequence, where G_0 (= 15.3 mT/mm) is the static gradient, the echo number (*NE*) is 4000, the echo spacing $\tau = 40\,\mu s$, and the number of saturation recovery sampling points (N_{SR}) is 21 or 11.

respiratory variation, and related MR imaging and NMR artifacts are absent from this system.

Simultaneous T_1 Measurement Using MR Relaxation Contrast Agent and Calcium Fluorescence Imaging

This hybrid optical-MR system enables simultaneous fluorescence imaging and MR measurements (20). It combines a single-sided NMR system and a wide-field fluorescence microscope with an objective having a long working distance. This system is briefly described in the Supporting Information (Supporting Information S1). Longitudinal MR relaxometry with an extracellular gadolinium-based MR relaxation contrast agent (CA), gadoteridol (ProHance [PH], Bracco Diagnostics, Princeton, NJ), was used to distinguish intracellular and extracellular water magnetization signals by increasing the extracellular water resonance's longitudinal relaxation rate constant (R_{1o}). A saturation-recovery (SR) MR sequence with 21 recovery times (t_1) was used to measure R_1 values (Fig. 2) at three CA concentrations (0, 2.5, and 5.0 mM) in the perfusing medium. Details of this MR sequence are provided in the Supporting Information (Supporting Information S2).

Experimental Design

In these experiments, the OCC was kept in an environmental chamber with constant and slow perfusion (30 mL/h) of oxygenated (95% O_2 + 5% CO_2) artificial cerebrospinal fluid (ACSF) (124 mM NaCl, 3.5 mM KCl, 10 mM glucose, 26.2 mM $NaHCO_3$, 0.3 mM NaH_2PO_4, 1.2 mM $CaCl_2$ and 1 mM $MgSO_4$). The perfusate temperature was kept constant at 34.0 °C (± 1.0 °C). PH and ouabain (ouabain octahydrate, Abcam, Inc., Cambridge, MA) were added directly to the perfusate, with the NaCl concentration adjusted to maintain constant ACSF osmolality.

To estimate normal water transcytolemmal cycling, a total of 102 OCC samples were studied, of which 16 were scanned with SR measurements at three PH concentrations (0, 2.5, and 5 mM) and the others at two PH concentrations (0 and 5 mM). For each OCC sample, a single SR acquisition was carried out at $[PH_o] = 0$ mM (scan time for a single acquisition was 21.0 min), while two SR acquisitions were carried out at $[PH_o] = 2.5$ or 5 mM (scan time for a single acquisition was 13.8 min). When a higher $[PH_o]$ was used, the apparent T_2 was continuously monitored via a CPMG sequence to confirm that the PH reached steady state in the OCC, which normally takes 20–25 min.

Ouabain experiments were carried out on eight OCC samples at $[PH_o] = 5$ mM with a faster acquisition (scan time for a single acquisition was 6.9 min; Supporting Information S2). The detailed experimental protocol was as follows: baseline with normal ACSF (four acquisitions, ~27.5 min), 1 mM ouabain (five acquisitions, ~34.4 min), washout with normal ACSF (seven acquisitions, ~48.3 min), all with 5 mM PH. Separate control experiments were carried out on six different organotypic culture slices, using the same experimental protocol but with the ouabain replaced with normal ACSF.

During these experiments, calcium images were also acquired simultaneously with MR measurements, with 1 × magnification, $8.8 \times 6.6\,mm^2$, field of view (FOV) 680 × 512 pixels, exposure of 100 ms, at 10 frames/s.

Details of calcium signal processing and statistical analysis are provided in the Supporting Information (Supporting Information S3).

T_1 Data Preprocessing and Analysis

In the MR SR experiments, the first four echoes in each CPMG echo train, which have systematic artifacts (21), were removed. Then, the average of the first thousand echoes in the remaining train was used as the signal intensity at each t_1. The number of echoes averaged was chosen to avoid including signals in the noise floor. In the baseline experiments at $[PH_o] = 2.5$ or 5 mM, the two repeated acquisitions were averaged to improve the signal-to-noise ratio (SNR).

The equilibrium (or fully relaxed) longitudinal magnetization, M_0, was assigned as that acquired at $t_1 = 10$ s at $[PH_o] = 0$ mM and that acquired at $t_1 = 5$ s at $[PH_o] = 2.5$ or 5 mM. The longitudinal magnetization at all other t_1 values, $M(t_1)$, was subtracted from and normalized by M_0. The quality $[M_0 - M(t_1)]/M_0$ was fitted with empirical single-exponential and bi-exponential models,

$$\frac{M_0 - M(t_1)}{M_0} = (1-\alpha)e^{-R'_1 t_1}, \quad [3]$$

$$\frac{M_0 - M(t_1)}{M_0} = (1-\alpha)[p'_{sm}e^{-R'_{1sm}t_1} + (1-p'_{sm})e^{-R'_{1lar}t_1}], \quad [4]$$

where $\cos^{-1}\alpha$ is the effective flip-angle of the saturation pulse, and R'_{1sm} and R'_{1lar} are the small and large apparent relaxation rate constants, respectively, and p'_{sm} is the apparent fractional intensity of the R'_{1sm} signal.

Two-Site-Exchange (2SX) Model

In this study, the SR data from OCCs were taken as the sums of signals from two water pools: intra- and extracellular water; all water magnetization within each pool was assumed to have a similar R_1. In this case, SR data were further analyzed with a two-site-exchange (2SX) model to determine the transcytolemmal water exchange kinetics with the following parameters: p_i. – the intracellular water mole fraction; k_{io}– (where τ_i [$\equiv 1/k_{io}$] is the intracellular water residence time), and r_{1PHo}– the effective

PH relaxivity in the overall extracellular space of the MR selective volume (V_{MR}), which is defined by (10):

$$r_{1PHo} = \frac{R_{1o} - R_{1ACSF}}{[PH_o]} \quad [5]$$

where R_{1o} is the R_1 in the extracellular space at $[PH_o]$ (it is assumed PH does not enter cells during the experimental time (1–2 h) (22), and R_{1ACSF} is the R_1 in free ACSF at $[PH_o] = 0$ mM. It is important to note that $p_i = (v_i - f_M)/(1 - f_M)$, where v_i and f_M are the volume fractions, respectively, of cytoplasm and spaces not accessible to mobile aqueous solutes (occupied by macromolecules) in V_{MR} (23); and $v_i = \rho\langle V\rangle$, where ρ and $\langle V\rangle$ are, respectively, the cell number density ("cellularity") and the mean individual cell volume. Because the tissue volume was so much smaller than V_{MR}, f_M did not change appreciably during our experiments.

The 2SX model predicts the SR data can be described with the bi-exponential model, Eq. [4], but with R'_{1sm}, R'_{1lar} and p'_{sm} expressed in terms of intrinsic parameters as follows (10,24,25):

$$R'_{1sm} = \frac{R_{1i} + R_{1o} + k_{io} + k_{oi} - \sqrt{(R_{1i} - R_{1o} + k_{io} - k_{oi})^2 + 4k_{io}k_{oi}}}{2}, \quad [6]$$

$$R'_{1lar} = \frac{R_{1i} + R_{1o} + k_{io} + k_{oi} + \sqrt{(R_{1i} - R_{1o} + k_{io} - k_{oi})^2 + 4k_{io}k_{oi}}}{2}, \quad [7]$$

$$p'_{sm} = \frac{(R_{1o} + k_{io} + k_{oi} - R'_{1sm})p_i - (-R'_{1lar} + R_{1o})(1 - p_i)}{R'_{1lar} - R'_{1sm}}, \quad [8]$$

where k_{oi} is the steady-state cellular influx rate constant. At equilibrium or steady-state (homeostasis), the principle of microscopic reversibility (detailed balance) (26) demands that

$$k_{io}/k_{oi} = k_{io}(a)/k_{oi}(a) = k_{io}(p)/k_{oi}(p) = (1 - p_i)/p_i. \quad [9]$$

The 2SX model was applied to SR data obtained at a single concentration, $[PH_o] = 5$ mM, to avoid any bias induced by different transverse relaxation quenching, i.e., the SR data were T_2-weighted because the effective echo time (TE) was finite (20 ms), and the extracellular water transverse magnetization relaxation rate constant (R_{2o}) is $[PH_o]$-dependent (27). Here, R_{1i} was fixed at 1.74 s^{-1} in Eqs. [6]–[8] for SR data obtained at the normal condition (i.e., no changes in V). The R_{1i} value was estimated from contrast agent-free human cortex T_1 data (28) under several reasonable assumptions: (1) the intra- and extracellular water are in the fast-exchange limit in that case, i.e., the detected $R'_1 = p_iR_{1i} + (1 - p_i)R_{1o}$; (2) $p_i = 0.80$ (3,29) R_{1o} is equal to the R_1 of free CSF in (28); and (4) R'_1 of rat cortex at 0.32T is estimated by fitting the human cortex T_1 data with the power law (28). The 2SX model was directly applied to the acquired MR signal, $M(t_1)$. Therefore, the three independent system parameters (p_i, k_{io}, and r_{1PHo}) involved in Eqs. [6–8], and two acquisition parameters in Eq. [4], M_0 and α, were also varied in the 2SX model.

In the ouabain and control experiments, the baseline data were also processed with the 2SX model using the same protocol. During the ouabain wash-in and washout phases, in which cell volume change was expected, the value of R_{1i} was adjusted on the basis of the following assumption (28):

$$R_{1i} = \frac{r_{1Mi}n_{Mi}}{V} + R_{1ACSF}, \quad [10]$$

where n_{Mi} is the number of millimoles of macromolecules (M) per cell volume, V, (in liters) and r_{1Mi} is the mean macromolecule relaxivity. Both r_{1Mi} and n_{Mi} are constants and independent of cell volume. V is linearly related to p_i with $V = [(1 - f_M)p_i + f_M]/\rho$, where f_M is a constant value that can be estimated from baseline p_i (17). In this way, R_{1i} will be explicitly a function of p_i. Therefore, alternatively, the relative V changes could also be quantitatively estimated via Eq. [10].

RESULTS

Intra- and Extracellular Water Signals Distinguished in NMR

Here, we demonstrate how an MRI contrast agent can help distinguish intra- and extracellular water by quantitative analysis of MR signals at various $[PH_o]$ values. In Figure 3, the semi-logarithmic SR decays, $[M_0 - M(t_1)]/M_0$, from ACSF only and OCC samples are displayed. The ACSF data are well fitted with the single-exponential function Eq. [3] with R'_1 estimated to be 0.46, 11.30, and 21.22 s^{-1} at $[PH_o] = 0$, 2.5 and 5.0 mM, respectively (Table 1). Therefore, the CA's longitudinal relaxivity in ACSF is 4.17 $s^{-1}mM^{-1}$ at 34°C (±1°C). At $[PH_o] = 0$ mM, the OCC data ($N = 16$) are also well fitted by a single-exponential model (Eq. [3]) with estimated $R'_1 = 0.60$ s^{-1}—slightly larger (but significant with $P = 2 \times 10^{-10}$) than that of ACSF, indicating the intracellular water magnetization R_1 must be larger than that of ACSF without PH.

At $[PH_o] = 2.5$ and 5.0 mM, the OCC SR data clearly depart from a single-exponential relaxation. They decay more slowly at longer t_1 than at shorter t_1. By using the empirical bi-exponential fit Eq. [4], the data from either $[PH_o] = 2.5$ or 5.0 mM are well approximated, suggesting that at least two water compartments exist in OCC. The parameters estimated are summarized in Table 1. The R'_{1lar} values are slightly smaller than the R'_1 values obtained from ACSF only, whereas R'_{1sm} showed no significant difference between $[PH_o] = 2.5$ and 5.0 mM ($p = 0.60$). Interestingly, p'_{sm} significantly decreased from 0.089 at $[PH_o] = 2.5$ mM to 0.064 at $[PH_o] = 5$ mM ($P = 0.004$ with paired Student's t-test). It should be a constant if there was no exchange (see below), or even increase because of greater transverse relaxation quenching of extracellular water magnetization.

Steady-State Transcytolemmal Water Exchange Exists in OCC

To demonstrate the existence of steady-state transcytolemmal water exchange in OCC, its effect on the MR SR decay signals was assessed by carrying out simulations. The analytical $[PH_o]$ dependences of the empirical bi-

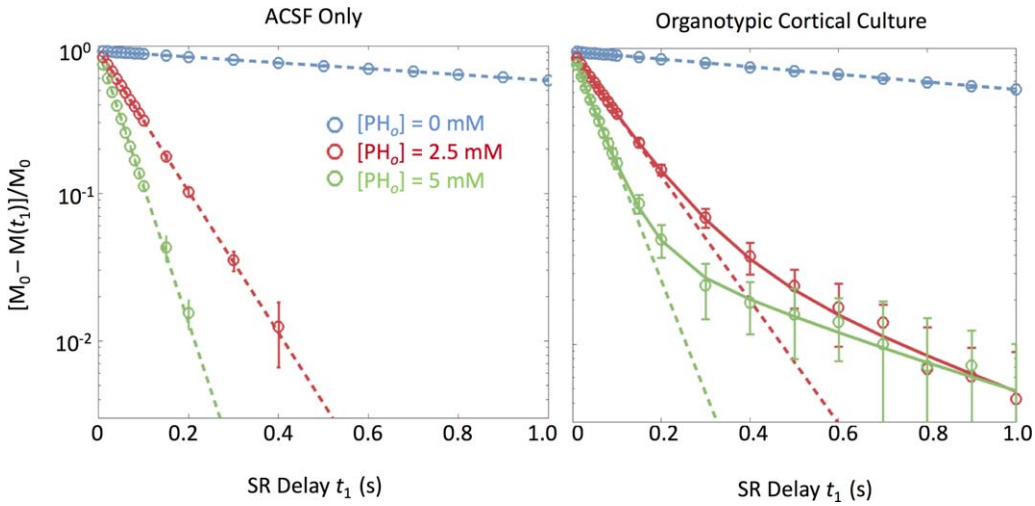

FIG. 3. The averaged SR data from ACSF only (left, $N = 6$) and OCCs (right, $N = 16$) at three [PH_o] values, in which the dashed and continuous curves are fitted with the empirical single- and bi-exponential expressions, Eqs. [3] and [4], respectively. The raw SR data are displayed as the mean (± standard deviation) at each t_1.

exponential Eq. [4] p'_{sm}, R'_{1sm}, and R'_{1lar} parameters were calculated from Eqs. [5]–[9] with the following 2SX parameters: $p_i = 0.07$, $R_{1i} = 1.74\ s^{-1}$, $R_{1ACSF} = 0.46\ s^{-1}$, and $r_{1PHo} = 4.00\ \ s^{-1}mM^{-1}$. These parameters were chosen to mimic the OCC case. The parameter k_{io} was varied from 0 to 4 s^{-1} and [PH_o] was varied from 0 mM to 6 mM. The intrinsic transverse relaxation rate constants of both intracellular and extracellular water magnetization were assumed to be zero.

In Figure 4, the analytical 2SX solutions are illustrated with p'_{sm}, R'_{1sm}, and R'_{1lar} plotted as functions of [PH_o] and k_{io}. Without any exchange, $k_{io} = 0\ s^{-1}$, both p'_{sm} and R'_{1sm} are [PH_o] independent (horizontal dashed lines). With exchange, both parameters are strongly dependent on [PH_o] and k_{io} values. At low [PH_o], p'_{sm} approaches 1.0 at all $k_{io} > 0\ s^{-1}$ (i.e., p'_{lar} vanishes). As [PH_o] increases, p'_{sm} decreases, and approaches p_i only at high [PH_o]. It is very important to note that p_i will be vastly overestimated ($p'_{sm} > p_i$) if k_{io} is assumed to be infinitely large, as is commonly done: k_{io} must be determined to get accurate p_i (and therefore, V). This has been independently verified in myocardium (30).

Table 1
Results of the Empirical Single- and Bi-Exponential Fits of ACSF and OCC SR Data at Three [PHo] Values

	[PH_o] (mM)	0	2.5	5
ACSF ($N = 6$)	R'_1 (s^{-1})	0.46 (±0.00)	11.30 (±0.08)	21.22 (±0.13)
OCCs ($N = 16$)	p'_{sm}	N.A.	0.089 (±0.010)	0.064 (±0.006)
	R'_{1sm} (s^{-1})	0.60 (±0.01)	2.88 (±0.20)	2.76 (±0.25)
	R'_{1lar} (s^{-1})		10.64 (±0.13)	19.88 (±0.21)

The data are displayed as the mean (±standard error of the mean).

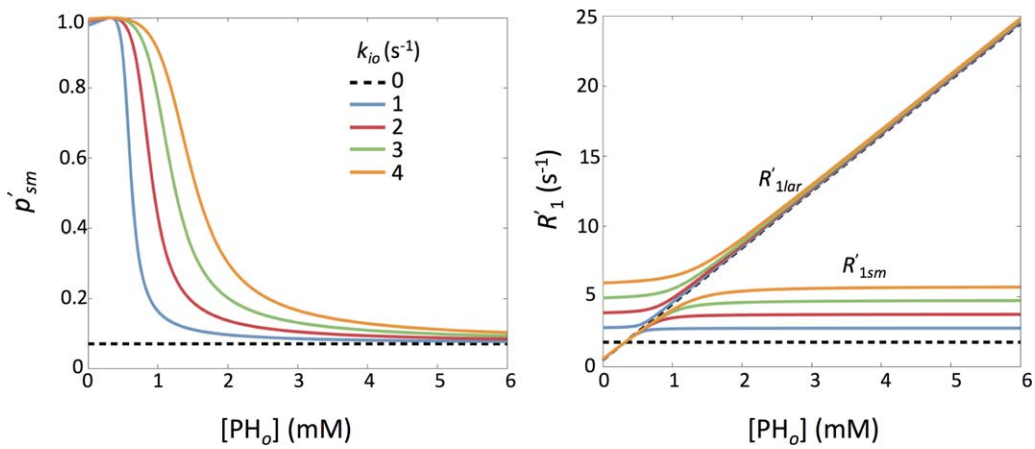

FIG. 4. Analytical solutions of p'_{sm} (left), R'_{1sm}, and R'_{1lar} (right) for the simulated 2SX system at various [PH_o] and exchange rate constant values (Eqs. [3]–[8]).

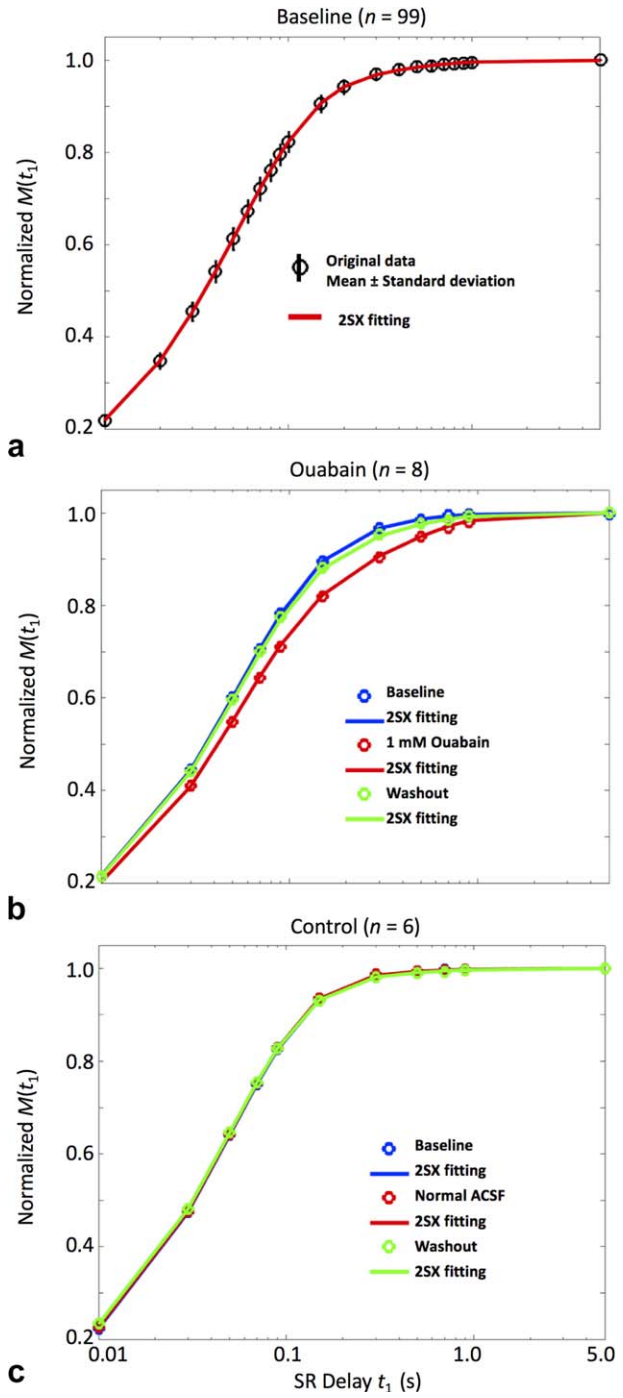

FIG. 5. (**a**) The 2SX-model fitting of the SR data from OCC ($[PH_o] = 5$ mM) in which the raw data are displayed as the mean (±standard deviation) error bars. (**b**,**c**) The 2SX model fittings of the MR SR data from ouabain (b), and ouabain control (c) studies during three phases: (I) baseline (blue, the average of the four acquisitions), (II) 1 mM ouabain (red, the average of the last three acquisitions), and (III) washout (green, the average of the last three acquisitions). The open circles represent the raw data, and the continuous curves represent the results from the 2SX model fittings. Table 2 gives the parameter values returned by the fittings.

On the other hand, the R'_{1lar} approaches R_{1o} while R'_{1sm} is almost constant at high $[PH_o]$ (i.e., $[PH_o] > 2$ mM). All the changing patterns in the experimental p'_{sm}, R'_{1sm}, and R'_{1lar} values confirm that steady-state transcytolemmal water exchange is evident in our OCC data.

The Baseline OCC Steady-State Cellular Water Efflux Rate Constant

The 2SX model was applied to the data obtained at a single CA concentration. Here, a total of 102 OCCs with $[PH_o] = 5.0$ mM were studied and analyzed with the 2SX model. Three were not included into the statistics because of their low cellularity ($p_i \leq 0.035$). The 2SX model fitted the SR data from OCCs ($N = 99$) without any systematic bias in the residuals, and reported the cellular water efflux rate constant to be 2.02 (±1.72) s^{-1} (Fig. 5a; Table 2).

NKA Inhibition by Ouabain

To further study the potential active mechanism of transcytolemmal water exchange, the OCC was briefly perfused with ouabain, a specific NKA inhibitor. As shown in Figure 6, in the control in which OCC was perfused with normal ACSF containing 5 mM PH, regular neuronal spike activity was observed for the entire recording period (~110 min): PH does not appear to affect neuronal function. This may be an important observation for the use of this CA in vivo. In the ouabain experiments, the intracellular calcium content increased and reached a maximum around 10 min after the start of the ouabain perfusion and then slowly decreased while ouabain was washed out. However, the intracellular calcium content was still greater than the baseline level after a 48-min washout with normal ACSF.

During ouabain perfusion, the SR data showed a significant response that depended on the SR delay t_1 (Fig. 6, bottom panel). The maximum changes in SR data were observed for $t_1 = 0.15$ s while no significant changes were observed in the control study at any t_1. The changes in the SR data reached a maximum by the third acquisition (~21 min) after ouabain introduction and remained constant, or decreased, until the onset of washout with normal ACSF.

To characterize the pathological changes in OCCs during ouabain addition, the 2SX model was applied to the data from each acquisition. In Figure 5b, the performance of the 2SX model is displayed for SR data acquired from three phases: (I) baseline (the average of the first four acquisitions), (II) 1 mM ouabain (the average of the last three acquisitions during ouabain perfusion), and (III) washout (the average of the last three acquisitions). In both the ouabain and control (Fig. 5C) experiments, the 2SX model well approximated the SR data from all three phases. In the ouabain experiments, the SR Phase II data themselves were clearly distinguishable from those at Phase I, whereas the washout with normal ACSF restored the SR data in Phase III. In the control, no significant changes in SR data were observed during these three phases. The fitted system parameter values for the ouabain baseline and ouabain phases (but not for the ouabain washout phase or ouabain control experiment) are also listed in Table 2.

The changes in the normalized 2SX model fitting parameters, p_i, $V^{1/3}$, and k_{io}, are shown in Figures 7

Table 2
Parameters From 2SX Model Fittings of OCC Data

Conditions	Intracellular water mole fraction: p_i	Water efflux rate constant: k_{io} (s^{-1})	Effective relaxivity of contrast agent in OCC: r_{1PHo} (s^{-1}/mM)
ACSF ($N = 99$)	0.074 (±0.026)	2.02 (±1.72)	3.87 (±0.25)
Ouabain baseline ($N = 8$)	0.099 (±0.025)	3.50 (±0.74)	3.86 (±0.22)
Ouabain (1 mM) ($N = 8$)	0.200 (±0.031)	1.85 (±0.45)	3.89 (±0.17)

and 8. The intracellular water mole fraction, p_i, increased by 110% (±36%) ($P = 7 \times 10^{-6}$) from the baseline during ouabain application in Phase II, but recovered to 18% (±37%) ($P = 0.28$) during ACSF washout in Phase III. Accordingly, the mean cell "diameter," being proportional to $V^{1/3}$, increased by only 23% (±6.7%) ($P = 7 \times 10^{-6}$) from the baseline during ouabain application, and recovered to 3.9% (±9.3%) ($P = 0.28$) during washout by ACSF. On the other hand, the cellular water efflux rate constant, k_{io}, decreased by 45% (±19%) ($P = 1 \times 10^{-3}$) from the baseline during ouabain application, but recovered to 24% (±31%) during ACSF washout ($P = 0.05$).

The V increase seems nearly simultaneous with the 45% k_{io} decrease. Although it is reasonable that P_W(p) in Eq. [2] remained unchanged, $\langle A/V \rangle$ might decrease as V increases. Assuming the cell shape does not change, $V^{-1/3}$ is a proportionate measure of $\langle A/V \rangle$ and the changes in k_{io}(p) from baseline to ouabain can be estimated from Eq. [2]:

$$\left\{\frac{k_{io}(\text{p, ouabain})}{k_{io}(\text{p, baseline})}\right\} = \left\{\frac{V_{\text{baseline}}}{V_{\text{ouabain}}}\right\}^{1/3} = \frac{1}{1.23} = 0.81. \quad [11]$$

In this case, k_{io}(p) decreased by 19%, and, therefore, k_{io}(a) independently decreased by 26%. In reality, the cell shape most likely also changes as the cell swells, and changes in $\langle A/V \rangle$ are almost certainly less than 19% and consequently k_{io}(a) decreased by more than 26% (see Discussion).

There were no significant changes observed in r_{1PHo} during either ouabain perfusion ($P = 0.62$) or washout by ACSF ($P = 0.39$, Table 2). In the control experiments ($N = 6$), no significant changes were observed in any fitting parameters (not tabulated).

DISCUSSION

The mechanisms of water transport across cell membranes in neuronal tissue are not well understood. In addition to net water flow across cell membranes in response to an osmotic gradient, intra- and extracellular water molecules are also in fast steady-state exchange. In neuronal tissue, the first-order efflux rate constant for the latter process averages 2 s^{-1}. Therefore, effectively, the entire intracellular water content is typically "turned-over" twice each second. It is important to note that this does not mean that the entire cell volume is flushed out twice each second but simply that two cell volumes of water are exchanged each second. Moreover, this steady-state transcytolemmal water exchange has an active component, which is driven by NKA activity.

Using a hybrid experimental set up, which allowed us to simultaneously measure intracellular calcium concentration via fluorescence imaging and transcytolemmal water transport kinetics with a novel, custom-designed NMR test system using a stable in vitro, neuronal OCC, we report three key findings: (a) perfusion with the paramagnetic MRI contrast agent gadoteridol (5 mM) did not significantly affect the coherent neuronal spiking of the

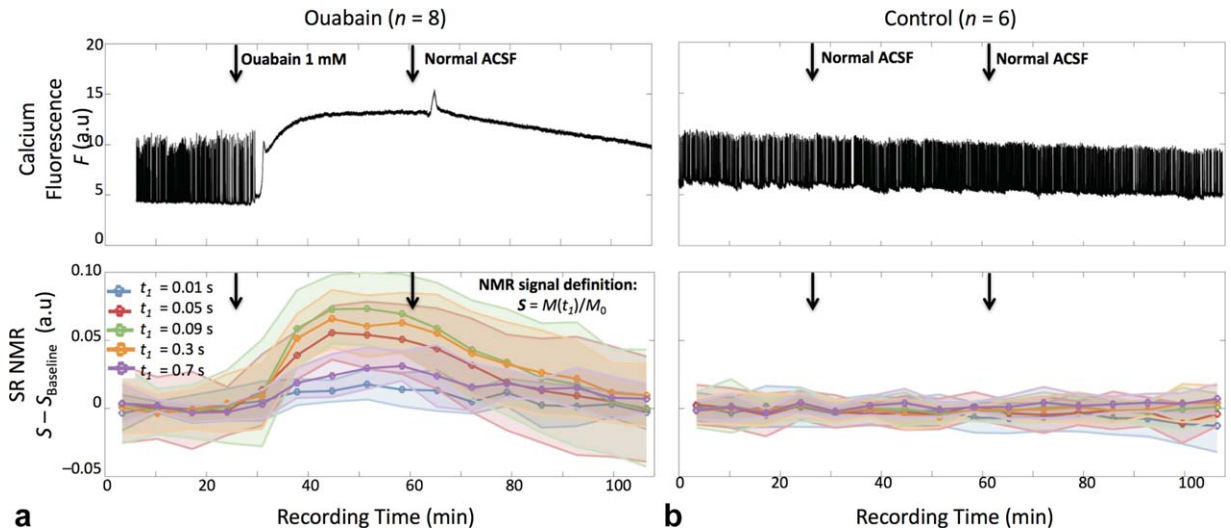

FIG. 6. The ouabain experiment. Top: representative intracellular calcium fluorescence traces (F) obtained during the transient introduction of 1 mM ouabain (**a**), and in the control study (**b**). Bottom: the normalized longitudinal magnetization at various t_1 values as function of recording time during ouabain introduction (a) and in control experiments (b).

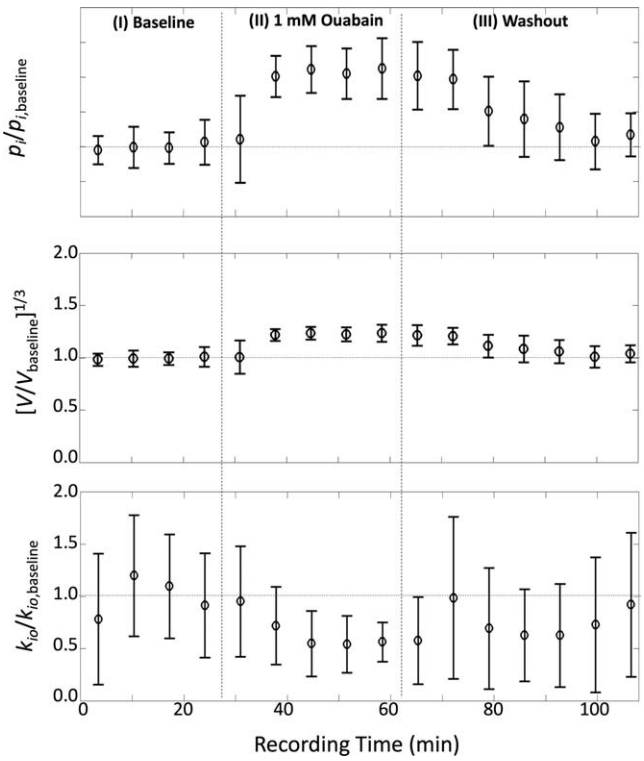

FIG. 7. Temporal profiles of the responses in p_i, $V^{1/3}$, and k_{io}, normalized by their averaged baseline values, in the ouabain experiments. The data are displayed as mean (±standard deviation).

tissue (Fig. 6) and enabled simultaneous steady-state cellular water efflux (k_{io}) and cell volume (V) measurement; (b) transient perfusion with 1 mM ouabain decreased the active k_{io} component and probably the passive component as well (Figs. 7 and 8); and (c) 1 mM ouabain increased [Ca_i^{2+}] (Fig. 6) and increased the mean cell volume (Figs. 7 and 8).

Quantitative measurements of transcytolemmal water exchange kinetics pose significant challenges. The only study on brain tissue in vivo, in an anesthetized state, used intracerebroventricular $Gd(DTPA)^{2-}$ infusions in rat (31), because MRI contrast agents do not normally cross the intact blood–brain barrier. That in vivo approach yielded $k_{io} = 1.8$ (±0.9) s^{-1}, which is consistent with our findings on rat brain cultures presented here ($k_{io} = 2.0$ (±1.7) s^{-1}). However, our k_{io} uncertainty is greater than in the in vivo measurement and when compared with other parameters (cf. Fig. 7 and Table 2). A major factor contributing to this increased uncertainty is the approximately one order of magnitude smaller intracellular water mole fraction, p_i, in our experiments compared to the in vivo study: (0.07 [±0.03] vs. 0.81 [±0.08]) (31). Specifically, the tissue volume of the cell culture is small compared with the MR detection volume. The extracellular water mole fraction unavoidably includes ACSF outside the tissue but inside the MR detection volume (20). Still, agreement of average k_{io} values is expected for this supra-intensive parameter (12): k_{io} is independent of the number of cells in V_{MR}, as long as the cell subpopulations remain the same. In such measures, errors are more prone to be random than systematic. Providing further support, recent in vitro studies report k_{io} values of 1.3 (±0.1) and 1.8 (±0.1) s^{-1} for bead-attached neurons and astrocytes, respectively (32). Although likely reduced by bead attachment, this tells us that k_{io} values differ for different cell types. This adds a biological variability for our tissue studies, because different preparations have different cell subpopulations.

Evidence for both the p_i and k_{io} variations is seen in Table 2. Eight tissue samples were used for the ouabain studies. However, during the baseline phase (no ouabain), the average p_i, 0.099, differs from that for 99 samples, 0.074. This is easily understandable because p_i is based on the fixed V_{MR} (see above). However, different tissue samples have different V_{tis} values: those chosen for ouabain baseline were larger. Likewise, the mean k_{io}

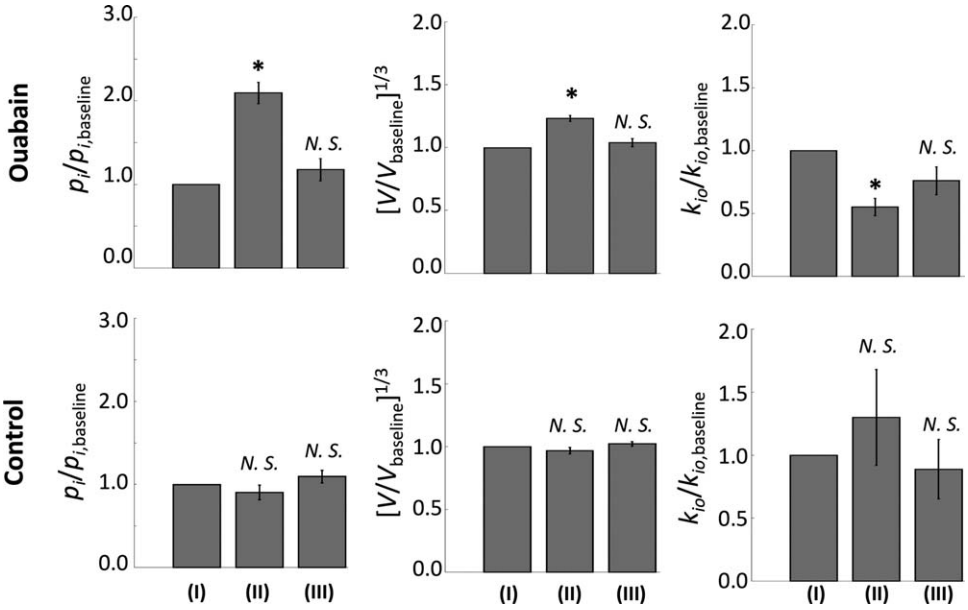

FIG. 8. Statistics of the normalized p_i, $V^{1/3}$, and k_{io} in three phases: (I) baseline (the average of the four acquisitions), (II) 1 mM ouabain (the average of the last three acquisitions), and (III) washout (the average of the last three acquisitions) in the ouabain and control experiments. The bar plots are displayed as means (±standard error of the mean). *$P < 0.05$ with paired Student's t-test compared with baseline values. N.S., not significant (i.e., $P \geq 0.05$).

for the ouabain-free baseline was 3.50 s^{-1}, whereas for 99 samples, it was 2.02 s^{-1}. The eight ouabain tissues likely were more astrocyte rich than the general OCC. The average over a very large number (99) of in vitro samples equals the in vivo case.

Transcytolemmal water exchange involves passive (k_{io}(p)) and active (k_{io}(a)) pathways, in which the former is dependent on cell morphology, size, and passive cell membrane water permeability, while the latter is dependent on water co-transporters driven by metabolic activity (Fig. 1). Ideally, we would like to perturb only one pathway without altering others. However, simultaneous changes (e.g., in cell morphology, volume) likely occur for any perturbation of membrane water transport, including NKA blockage with its specific inhibitor, ouabain (11). In other words, the k_{io}(p) might also be altered during perturbation of k_{io}(a), and we must also characterize changes in both k_{io}(p) and the total exchange rate constant k_{io} to be able to quantify k_{io}(a).

In this study, we demonstrate a quantitative method to characterize the transcytolemmal water exchange kinetics (k_{io}) and mean cellular volume (V) simultaneously, by using an MR relaxation CA, which cannot penetrate cell membranes, to distinguish extracellular and intracellular water MR signals. Our simultaneous and independent determination of k_{io} and V allowed us, to our knowledge for the first time, to ascertain changes in k_{io}(p) and k_{io}, and therefore k_{io}(a).

Because NKA is such a vital enzyme, it has a substantial turnover number (up to 250 s^{-1}) (33). It is also generally highly expressed. For a spherical cell with $V = 2$ pL, there could be as many as 8×10^6 NKA molecules in the cell membrane (34). If there were 10^5 cells/μL in the tissue (11), there could be 2×10^5 cells, and 2×10^{12} NKA molecules (3 pmol), in our typical tissue sample V_{tis} (1.6 μL; Supporting Information S4). This amounts to 2 μM in the tissue, and 1 μM in our MR-sensitive volume ($V_{MR} = 2.5$ μL; Supporting Information S4). Even though this is a conservatively large NKA concentration estimate, it is small compared with the 1 mM ouabain that perfused the tissue. Therefore, it is a good assumption that $^{c}MR_{NKA}$, and therefore k_{io}(a), goes to zero (Eq. [2]) during the ouabain perfusion (a 100% k_{io}(a) reduction). Ouabain probably saturates the NKA sites. The K_m for ouabain is near 0.1 μM (33). This would mean that $k_{io} = 1.85$ s^{-1} during the perfusion of ouabain (Table 2) represents k_{io}(p) during ouabain, for those tissues chosen.

We find a 45% overall k_{io} decrease and a seemingly simultaneous 23% increase in the cube root of V (26% of $p_i^{1/3}$ in Table 2), on brief exposure of OCC to ouabain. These results indicate the value of k_{io}(p) was decreased by 19% (Eq. [11]). This, in turn, suggests that k_{io}(p) at the ouabain baseline was 2.3 s^{-1}. For the yeast cell, $k_{io} \rightarrow 1.2$ s^{-1} when the intracellular NKA substrate concentration $[ATP_i] \rightarrow 0$ (10). Therefore, this likely represents k_{io}(p) for the yeast.

If, at the ouabain baseline, k_{io} is 3.5 s^{-1} (Table 2) and k_{io}(p) is 2.3 s^{-1}, k_{io}(a) is 1.2 s^{-1}, or 34% of the baseline k_{io}. In reality, the cell shape also changes during cell swelling, which would almost certainly make the $\langle A/V \rangle$ change less than the 19% $V^{-1/3}$ decrease. The claustrophobia ratio $\langle A/V \rangle$ value differs for different shapes, e.g., $4/d$ for cylinders and $6/d$ for spheres and cubes, where d is the cylinder or sphere diameter and the cube edge, respectively. Generally, cell swelling involves a change toward a more spheroidal shape. It has been shown directly that 10 min of 0.1 mM ouabain perfusion causes some neuronal cell body swelling along with pronounced "beading" of neuronal dendrites (35). This suggests that neuronal process segments transition from cylindrical to more spherical shape and their $<A/V>$ coefficients could increase by up to 50% (from $4/d$ to $6/d$). Similarly, glia have been reported to become more spherical. It may be that, in general, A changes almost nullify V changes, leaving k_{io}(p) (Eq. [2]) little changed. If this is the case, it means k_{io}(p) is 1.9 s^{-1} at the ouabain baseline and that k_{io}(a), 1.6 s^{-1}, accounts for 45% of the homeostatic steady-state trans-membrane water flux.

The decrease in k_{io}(a) by ouabain further confirms our hypothesis that NKA activity contributes to active transcytolemmal water cycling (Fig. 1). In addition, ouabain increased intracellular calcium concentration, $[Ca_i^{2+}]$, and the cell volume. These latter effects might be because of increases in $[Na_i^+]$ resulting from a decrease in MR_{NKA} pumping but a continued Na^+ influx (transporters III, Fig. 1). The resulting decreased transcytolemmal $[Na^+]$ gradient could further increase cytoplasmic osmolality, which will cause a volume increase (36). That the V increase may slightly lag behind the k_{io} decrease (Fig. 7) could suggest k_{io} causality. There should, as well, be cell membrane depolarization, because the $[K^+]$ gradient will also be quickly diminished (37). Such cell membrane depolarization might increase $[Ca_i^{2+}]$ by opening voltage-gated Ca^{2+} channels, decreasing the voltage-sensitive Mg^{2+} block of the NMDA receptor (38,39) and disrupting the functionality of the Na_o^+/Ca_i^{2+} exchanger, which dominates normal Ca^{2+} efflux (40). During washout with ACSF, fast recovery of both cell volume and k_{io} (Fig. 7) suggest reversible ouabain binding to the NKA pump and fast removal of Na^+ by the NKA pump (36). The relatively slow $[Ca_i^{2+}]$ decrease (Fig. 6) during washout suggests that $[Na_i^+]$, which dominates the speed of the Na_o^+/Ca_i^{2+} exchanger, might not have recovered to basal levels during our recording time (40). An intriguing alternative possibility is that the ouabain washout is not so fast, but the activity of the other primary active ion pump, Ca^{2+}-ATPase (PMCA), ramps up and increases k_{io}. After $[Ca_i^{2+}]$ increases (Fig. 6), there are now considerable concentrations of both PMCA substrates, ATP_i and Ca_i^{2+}. Because it is an ion pump, Ca^{2+}-ATPase will be coupled to other ion transporters (Fig. 1), and it is possible this also can drive k_{io}(a).

Transcytolemmal water exchange kinetics have been well established in red blood cells ($k_{io} \sim 100$ s^{-1}) (27,41–43), almost two orders of magnitude faster than our results on brain neuronal tissue. The reasons underlying this finding might be the following: (a) red blood cells are smaller than brain cortical cells (e.g., neurons, astrocytes), i.e., red blood cells have a larger surface-to-volume ratio, which can increase k_{io}(p) (Eq. [2]); and (b) aquaporin water channels are highly expressed on red

blood cells, whereas no such water channels have been discovered on neuronal membranes (44,45), a major cell type in OCC, although they are present in glial cells (1).

It is interesting that the effective MRI contrast agent relaxivity, r_{1PHo}, is reduced by 7% from its value in ACSF (3.87/4.17). In the Supporting Information (Supporting Information S4), we show this indicates that PH concentration in the tissue interstitium, $[PH_o]$, is considerably reduced (possibly by more than 50%) from that in the perfusing solution. This has important consequences for traditional tracer interpretations ("indicator dilutation") of (dynamic-contrast-enhanced) DCE-MRI data, although it does not affect the k_{io} and p_i determinations here.

The ouabain-induced 45% k_{io} decrease we find is quite comparable to the 39% apparent water diffusion coefficient (ADC) decrease within 15 min of direct ouabain application to the in vivo rat brain (46) and that, in turn, is quite comparable to the typical 30% acute ADC decrease seen with human stroke (47). This is consistent with the hypothesis (10) that the ADC manifestation of stroke is more likely because of a decrease in Na^+-K^+-ATPase activity caused by O_2 deficiency than to cell swelling. The commonly invoked cell swelling mechanism has been shown inconsistent with a number of other facts as well (47).

CONCLUSIONS

We quantitatively assessed the transcytolemmal water exchange kinetics of rat brain organotypic cortical cultures in healthy and pathological conditions, with the latter induced by blocking the Na^+-K^+-ATPase pump. The results confirm that the cellular water efflux rate constant (k_{io}) of healthy rat brain cortical cells is near 2 s^{-1}. This study showed a global intracellular volume increase during ouabain Na^+-K^+-ATPase blockage with intracellular Ca^{2+} accumulation. This finding could represent that the mean cell volume increases for neurons, for glia, or—most likely—for both. More interestingly, blockage of the NKA pump significantly reduces the active transcytolemmal water exchange. These new findings may provide important clues not only for the interpretation of some MRI biomarkers of disease, but also for understanding some essential physiological processes underlying these diseases (e.g., cerebral ischemia).

ACKNOWLEDGMENTS

R.B. and P.J.B. were supported by the Intramural Research Program (IRP) of the Eunice Kennedy Shriver National Institute of Child Health and Human Development, NIH. We thank our colleague Craig Steward for helping prepare organotypic cultures. C.S.S. acknowledges Drs. Craig Jahr, Thomas Barbara, Christopher Kroenke, Deborah Burstein, Robert Balaban, and Suzanne Scarlata for stimulating discussions, and the NIH (UO1-CA154602 and R44-CA180425) and the Paul G. Allen Family Foundation (grant 12079) for support. D.P. was supported by the IRP of the National Institute of Mental Health, NIH.

REFERENCES

1. Papadopoulos MC, Verkman AS. Aquaporin water channels in the nervous system. Nat Rev Neurosci 2013;14:265–277.
2. Risher WC, Andrew RD, Kirov SA. Real-time passive volume responses of astrocytes to acute osmotic and ischemic stress in cortical slices and in vivo revealed by two-photon microscopy. Glia 2009; 57:207–221.
3. Shepherd TM, Flint JJ, Thelwall PE, Stanisz GJ, Mareci TH, Yachnis AT, Blackband SJ. Postmortem interval alters the water relaxation and diffusion properties of rat nervous tissue--implications for MRI studies of human autopsy samples. Neuroimage 2009;44:820–826.
4. Buckley DL, Bui JD, Phillips MI, Zelles T, Inglis BA, Plant HD, Blackband SJ. The effect of ouabain on water diffusion in the rat hippocampal slice measured by high resolution NMR imaging. Magn Reson Med 1999;41:137–142.
5. Manley GT, Binder DK, Papadopoulos MC, Verkman AS. New insights into water transport and edema in the central nervous system from phenotype analysis of aquaporin-4 null mice. Neuroscience 2004;129:981–989.
6. Liang D, Bhatta S, Gerzanich V, Simard JM. Cytotoxic edema: mechanisms of pathological cell swelling. Neurosurg Focus 2007;22:E2.
7. Badaut J, Ashwal S, Adami A, Tone B, Recker R, Spagnoli D, Ternon B, Obenaus A. Brain water mobility decreases after astrocytic aquaporin-4 inhibition using RNA interference. J Cereb Blood Flow Metab 2011;31:819–831.
8. Day RE, Kitchen P, Owen DS, Bland C, Marshall L, Conner AC, Bill RM, Conner MT. Human aquaporins: regulators of transcellular water flow. Biochim Biophys Acta 2014;1840:1492–1506.
9. Ye RG, Verkman AS. Simultaneous optical measurement of osmotic and diffusional water permeability in cells and liposomes. Biochemistry 1989;28:824–829.
10. Zhang Y, Poirier-Quinot M, Springer CSS, Balschi JAA. Active transplasma membrane water cycling in yeast is revealed by NMR. Biophys J 2011;101:2833–2842.
11. Springer CS, Li X, Tudorica LA, Karen YO, Nicole R, Stephen YC, Arpana MN, Megan LH, Aneela A, William DR, Wei H. Intratumor mapping of intracellular water lifetime: metabolic images of breast cancer? NMR Biomed 2014;27:760–773.
12. Rooney WD, Li X, Sammi MK, Bourdette DN, Neuwelt EA, Springer CS. Mapping human brain capillary water lifetime: high-resolution metabolic neuroimaging. NMR Biomed 2015;28:607–623.
13. Shinoda T, Ogawa H, Cornelius F, Toyoshima C. Crystal structure of the sodium–potassium pump at 2.4 Å resolution. Nature 2009;459: 446–450.
14. Zeuthen T. Water-transporting proteins. J Membr Biol 2010;234:57–73.
15. Illarionova NB, Gunnarson E, Li Y, Brismar H, Bondar A, Zelenin S, Aperia A. Functional and molecular interactions between aquaporins and Na,K-ATPase. Neuroscience 2010;168:915–925.
16. Rand RP. Probing the role of water in protein conformation and function. Philos Trans R Soc Lond B Biol Sci 2004;359:1277–1285.
17. Vinnakota KC, Bassingthwaighte JB. Myocardial density and composition: a basis for calculating intracellular metabolite concentrations. Am J Physiol Heart Circ Physiol 2004;286:H1742–H1749.
18. Stewart CV, Plenz D. Homeostasis of neuronal avalanches during postnatal cortex development in vitro. J Neurosci Methods 2008;169: 405–416.
19. Plenz D, Stewart CV, Shew W, Yang H, Klaus A, Bellay T. Multi-electrode array recordings of neuronal avalanches in organotypic cultures. J Vis Exp 2011:e2949.
20. Bai R, Klaus A, Bellay T, Stewart C, Pajevic S, Nevo U, Merkle H, Plenz D, Basser PJ. Simultaneous calcium fluorescence imaging and MR of ex vivo organotypic cortical cultures: a new test bed for functional MRI. NMR Biomed 2015;28:1726–1738.
21. Casanova F, Perlo J, Blümich B. Single-sided NMR. Berlin: Springer; 2011.
22. Preston E, Foster DO. Diffusion into rat brain of contrast and shift reagents for magnetic resonance imaging and spectroscopy. NMR Biomed 1993;6:339–344.
23. Li X, Rooney WD, Springer CS. A unified magnetic resonance imaging pharmacokinetic theory: intravascular and extracellular contrast reagents. Magn Reson Med 2005;54:1351–1359.
24. Landeghem MVAN, Haber A. Analysis of multisite 2D relaxation exchange NMR. Concepts Magn Reson Part A 2010;36A:153–169.

25. Mitchell J, Griffith JD, Collins JHP, Sederman AJ, Gladden LF, Johns ML. Validation of NMR relaxation exchange time measurements in porous media. J Chem Phys 2007;127:234701.
26. Daniels F, Alberty RA. Physical chemistry, Fourth Edition. New York: John Wiley & Sons; 1975. p. 314–315.
27. Wilson GJ, Springer CS, Bastawrous S, Maki JH. Human whole blood ^1H_2O transverse relaxation with gadolinium-based contrast reagents: magnetic susceptibility and transmembrane water exchange. Magn Reson Med 2017;77:2015–2027.
28. Rooney WD, Johnson G, Li X, Cohen ER, Kim SG, Ugurbil K, Springer CS. Magnetic field and tissue dependencies of human brain longitudinal 1H2O relaxation in vivo. Magn Reson Med 2007;57:308–318.
29. Syková E, Nicholson C. Diffusion in brain extracellular space. Physiol Rev 2008;88:1277–1340.
30. Coelho-Filho OR, Mongeon FP, Mitchell R, Moreno H, Nadruz W, Kwong R, Jerosch-Herold M. Role of transcytolemmal water-exchange in magnetic resonance measurements of diffuse myocardial fibrosis in hypertensive heart. Circ Cardiovasc Imaging 2013;6:134–141.
31. Quirk JD, Bretthorst GL, Duong TQ, Snyder AZ, Springer CS, Ackerman JJH, Neil JJ. Equilibrium water exchange between the intra- and extracellular spaces of mammalian brain. Magn Reson Med 2003;50:493–499.
32. Yang DM, Huettner JE, Bretthorst GL, Neil JJ, Garbow JR, Ackerman JJH. Intracellular water preexchange lifetime in neurons and astrocytes. Magn Reson Med 2018;79:1616–1627.
33. Baker PF, Willis JS. Binding of the cardiac glycoside ouabain to intact cells. J Physiol 1972;224:441–462.
34. Baker PF, Willis JS. Inhibition of the sodium pump in squid axons by cardiac glycosides: dependence on extracellular ions and metabolism. J Physiol 1972;224:463–475.
35. Douglas HA, Callaway JK, Sword J, Kirov SA, Andrew RD. Potent inhibition of anoxic depolarization by the sodium channel blocker dibucaine. J Neurophysiol 2011;105:1482–1494.
36. Strange K. Ouabain-induced cell swelling in rabbit cortical collecting tubule: NaCl transport by principal cells. J Membr Biol 1989;107:249–261.
37. Balestrino M, Young J, Aitken P. Block of (Na+,K+)ATPase with ouabain induces spreading depression-like depolarization in hippocampal slices. Brain Res 1999;838:37–44.
38. Nowak L, Bregestovski P, Ascher P, Herbet A, Prochiantz A. Magnesium gates glutamate-activated channels in mouse central neurones. Nature 1984;307:462–465.
39. Mayer ML, Westbrook GL, Guthrie PB. Voltage-dependent block by Mg2 + of NMDA responses in spinal cord neurones. Nature 1984;309:261–263.
40. Koch R, Barish M. Perturbation of intracellular calcium and hydrogen ion regulation in cultured mouse hippocampal neurons by reduction of the sodium ion concentration gradient. J Neurosci 1994;14:2583–2593.
41. Herbst MD, Goldstein JH. A review of water diffusion measurement by NMR in human red blood cells. Am J Physiol 1989;256:C1097–C1104.
42. Wilson GJ, Woods M, Springer CS, Bastawrous S, Bhargava P, Maki JH. Human whole-blood 1H2O longitudinal relaxation with normal and high-relaxivity contrast reagents: influence of trans-cell-membrane water exchange. Magn Reson Med 2014;72:1746–1754.
43. Li JG, Stanisz GJ, Henkelman RM. Integrated analysis of diffusion and relaxation of water in blood. Magn Reson Med 1998;40:79–88.
44. Agre P, King LS, Yasui M, Guggino WB, Ottersen OP, Fujiyoshi Y, Engel A, Nielsen S. Aquaporin water channels—from atomic structure to clinical medicine. J Physiol 2002;542:3–16.
45. Andrew RD, Labron MW, Boehnke SE, Carnduff L, Kirov SA. Physiological evidence that pyramidal neurons lack functional water channels. Cereb Cortex 2007;17:787–802.
46. Veldhuis WB, van der Stelt M, Delmas F, Gillet B, Veldink GA, Vliegenthart JFG, Nicolay K, Bär PR. In vivo excitotoxicity induced by ouabain, a Na+/K+-ATPase inhibitor. J Cereb Blood Flow Metab 2003;23:62–74.
47. Ackerman JJH, Neil JJ. The use of MR-detectable reporter molecules and ions to evaluate diffusion in normal and ischemic brain. NMR Biomed 2010;23:725–733.

SUPPORTING INFORMATION

Additional Supporting Information may be found in the online version of this article.

Data S1. Simultaneous calcium fluorescence microscopy and NMR.
Data S2. T_1 measurement with MR relaxation contrast agent.
Data S3. Calcium signal processing and statistics.
Data S4. MRI Contrast Agent Distribution in Tissue.